

Eukaryotic Catalase-Peroxidase: The Role of the Trp-Tyr-Met Adduct in Protein Stability, Substrate Accessibility, and Catalysis of Hydrogen Peroxide Dismutation

Bernhard Gasselhuber,[†] Xavi Carpéna,[‡] Michael M. H. Graf,[§] Katharina F. Pirker,[†] Andrea Nicolussi,[†] Axel Sündermann,[§] Stefan Hofbauer,^{||} Marcel Zamocky,^{†,‡} Paul G. Furtmüller,[†] Christa Jakopitsch,[†] Chris Oostenbrink,[§] Ignacio Fita,[‡] and Christian Obinger*,[†]

[†]Department of Chemistry, Division of Biochemistry, BOKU-University of Natural Resources and Life Sciences, Muthgasse 18, A-1190 Vienna, Austria

[‡]Institut de Biología Molecular (IBMB-CSIC), Parc Científic de Barcelona, Baldiri Reixac 10-12, 08028 Barcelona, Spain

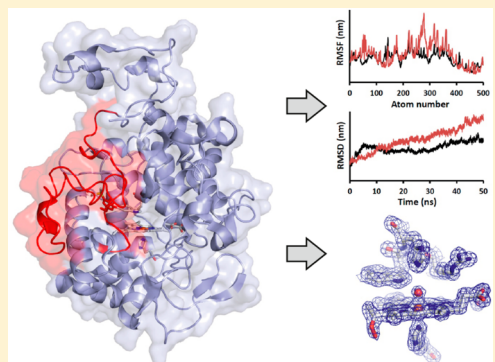
[§]Department of Material Sciences and Process Engineering, Institute for Molecular Modeling and Simulation, BOKU-University of Natural Resources and Life Sciences, Muthgasse 18, A-1190 Vienna, Austria

^{||}Department for Structural and Computational Biology, Max F. Perutz Laboratories, University of Vienna, Campus Biocenter 5, A-1030 Vienna, Austria

[†]Institute of Molecular Biology, Slovak Academy of Sciences, Dubravská cesta 21, SK-84551 Bratislava, Slovakia

S Supporting Information

ABSTRACT: Recently, it was demonstrated that bifunctional catalase-peroxidases (KatGs) are found not only in archaea and bacteria but also in lower eukaryotes. Structural studies and preliminary biochemical data of the secreted KatG from the rice pathogen *Magnaporthe grisea* (MagKatG2) suggested both similar and novel features when compared to those of the prokaryotic counterparts studied so far. In this work, we demonstrate the role of the autocatalytically formed redox-active Trp140-Tyr273-Met299 adduct of MagKatG2 in (i) the maintenance of the active site architecture, (ii) the catalysis of hydrogen peroxide dismutation, and (iii) the protein stability by comparing wild-type MagKatG2 with the single mutants Trp140Phe, Tyr273Phe, and Met299Ala. The impact of disruption of the covalent bonds between the adduct residues on the spectral signatures and heme cavity architecture was small. By contrast, loss of its integrity converts bifunctional MagKatG2 to a monofunctional peroxidase of significantly reduced thermal stability. It increases the accessibility of ligands due to the increased flexibility of the KatG-typical large loop 1 (LL1), which contributes to the substrate access channel and anchors at the adduct Tyr. We discuss these data with respect to those known from prokaryotic KatGs and in addition present a high-resolution structure of an oxoiron compound of MagKatG2.



Catalase-peroxidases (KatGs) are unique posttranslationally modified heme *b* peroxidases that are able to efficiently dismutate hydrogen peroxide like monofunctional catalases.¹ KatG-typical residues that were shown by mutagenesis experiments to be required for the catalytic process include the triad of three distal side residues, namely, Trp140, Tyr273, and Met299 [extracellular *Magnaporthe grisea* KatG (MagKatG2) numbering throughout],^{2–4} with Trp140 stacking ~3.4 Å above the heme. Crystal structures^{5–9} and mass spectrometric analysis^{10,11} demonstrated the existence of covalent bonds between Trp140 ($C\gamma 2$) and the adjacent Tyr273 ($C\epsilon 1$) as well as between Tyr273 ($C\epsilon 2$) and the sulfur of Met299. Moreover, Tyr273 is part of a KatG-typical insertion denominated large loop 1 (LL1) that consists of ~40 amino acids of a conserved sequence pattern and contributes to the

architecture of the narrow and tapered substrate channel of KatG.

In prokaryotic KatGs, it has been demonstrated that this peculiar Trp-Tyr-Met adduct, in its entirety, is fully essential for the catalase activity and that its presence has a strong influence on the electronic structure and spectroscopic signatures of the redox intermediates of KatG. The latter are completely different compared to monofunctional peroxidases or catalases.^{4,12–17} Finally, upon application of freeze-quench electron paramagnetic resonance spectroscopy, it was demonstrated that the adduct participates in the redox reaction and that a [Trp-Tyr-Met] \bullet^+ radical species is central in the efficient (pseudo-

Received: July 23, 2015

Revised: August 20, 2015

Published: August 20, 2015



catalytic turnover and dioxygen release of KatG.^{18–20} Thus, it is this second redox-active cofactor besides heme *b* that mainly distinguishes bifunctional KatG from its phylogenetically related monofunctional peroxidases.²¹ The latter have an almost negligible catalytic activity and are inhibited with time by hydrogen peroxide in the absence of exogenous electron donors.²²

Because KatGs initially were thought to be of bacterial and archaeal origin²³ exclusively, as well as because of the importance of *Mycobacterium tuberculosis* KatG (*Mt*KatG) in activation of the antitubercular prodrug isoniazid, detailed mechanistic studies were performed on prokaryotic KatGs only. Phylogenetic analysis suggested that the evolution of the peroxidase-catalase superfamily, which except for KatGs is comprised of monofunctional peroxidases only, started with predecessors of homodimeric KatGs with two domains per subunit, namely, an N-terminal domain, containing both a heme *b* and a Trp-Tyr-Met adduct, and a C-terminal domain, lacking both redox cofactors.^{1,24} Finally, it was demonstrated that extant KatGs are also present in protozoa (including marine heterotrophs and unicellular photosynthetic algae) and ascomycetous fungi. Most of the fungal KatGs are located intracellularly,^{25,26} but in pathogenic fungi, extracellular and secreted KatGs are additionally found,²⁷ suggesting that they are involved in the defense against the oxidative burst produced by infected plants.²⁸

Recently, we succeeded in determining the first crystal structure of a eukaryotic KatG [i.e., secreted KatG from *M. grisea* (*Mag*KatG2)] at 1.55 Å resolution.⁸ Its structure was similar in many respects to those of prokaryotic and archaeabacterial KatGs but presented in addition a number of novel features that are fully conserved in secreted eukaryotic KatGs. Compared to prokaryotic KatGs, *Mag*KatG2 exhibits a significantly higher conformational and thermal stability because of intersubunit disulfide bridges that contribute to subunit intertwining. In this work, we examine the role of the covalent Trp-Tyr-Met adduct of *Mag*KatG2 in (i) protein stability and dynamics, (ii) maintenance of the architecture of the main substrate channel, and (iii) hydrogen peroxide dismutation activity and discuss similarities and differences with findings from prokaryotic KatGs. In addition, we present the structure of an oxoiron compound of secreted *Mag*KatG2 at 1.6 Å resolution produced by crystal soaking with peroxyacetic acid and compare it with that of the ferric high-spin form.

MATERIALS AND METHODS

Cloning, Site-Directed Mutagenesis, Heterologous Expression, and Protein Purification. Cloning and expression of recombinant wild-type catalase-peroxidase from *M. grisea* (wild type and point mutants) in *Escherichia coli* strain BL21(DE3) Star (Invitrogen) were described recently.²⁷

Point mutants in the cloned wild-type gene were introduced with a polymerase chain reaction (PCR)-based site-directed mutagenesis kit (QuikChange Lightning Kit from Agilent Technologies) using two complementary oligonucleotides with the planned mutation in the middle of their sequence (Supplemental Table 1). The PCR program included initial denaturation at 95 °C for 2 min, 18 cycles of 20 s at 98 °C, 10 s at 60 °C, and 5 min at 68 °C, and a final amplification for 5 min at 68 °C (QuickChange Lightning Enzyme). In the next step, the restriction enzyme DpnI was added to all amplification reactions to digest the methylated or hemimethylated parental DNA. Reaction mixtures were incubated at 37 °C for at least 5 min

and directly transformed in competent *E. coli* BL21(DE3) Star cells via heat shock. Selected transformants grown on LB-agar plates were picked, cultivated, and analyzed by sequencing of the plasmid DNA (LGC genomics).

For protein expression, *E. coli* cells were grown in 500 mL of M9ZB medium in 2 L Erlenmeyer flasks inoculated with a freshly prepared overnight culture. M9ZB medium was supplemented with ampicillin (100 µg mL⁻¹) and 40 mg L⁻¹ hemin prior to induction. After the OD₆₀₀ had reached 0.6 in an agitated culture at 37 °C, recombinant protein expression was induced by sterile addition of either 0.5% (w/v) lactose or 0.5 mM isopropyl β-D-1-thiogalactopyranoside. The cultivation temperature was lowered to 16 °C during overnight protein expression. The cells were harvested by centrifugation, and cell pellets were frozen at -30 °C and stored until they were purified.

Cell pellets were resuspended in 50 mM sodium phosphate buffer (pH 8.0) containing 500 mM NaCl and the protease inhibitor phenylmethanesulfonyl fluoride and homogenized by ultrasonication. The crude homogenate was clarified by centrifugation (>20000g), and cell debris and the residual pellet were discarded. The clear supernatant was loaded onto a 20 mL Chelating Sepharose Fast Flow Column (GE Healthcare). Prior to the sample being loaded, the Chelating Sepharose was loaded with Ni²⁺ ions and equilibrated with 50 mM phosphate buffer (pH 8.0) containing 500 mM sodium chloride. His-tagged proteins were eluted with a linear gradient of 0 to 500 mM imidazole in 50 mM sodium phosphate (pH 7.5) containing 500 mM NaCl. Eluted fractions were collected automatically and checked by UV-vis spectroscopy. The KatG-containing fractions were pooled accordingly and concentrated by centrifugation with Centriprep 30K spin membranes (Millipore).

Additionally, heme proteins were purified using a hydroxylapatite column (25 mL, Sigma Chemicals or Bio-Rad). After equilibration with 5 mM phosphate buffer (pH 7.5), the column was loaded with the prepurified protein. After being washed with at least 3 column volumes of equilibration buffer, the protein was eluted by increasing the phosphate concentration in a stepwise fashion. Eluted protein was collected to separate the high-spin heme fractions from the low-spin fractions. High-spin protein fractions were pooled and concentrated as mentioned previously. Concentrated protein samples were stored at -80 °C.

For evaluation of purification success, protein electrophoresis was performed with NuPAGE Novex Bis-Tris gradient gels (4 to 12%) with 15 wells (Invitrogen) (running buffer of MOPS-SDS). Gels were stained with Coomassie Brilliant Blue (Sigma-Aldrich) or immunoblotted onto a nitrocellulose membrane (Amersham Biosciences) for detection of *Mag*KatG2 by using a penta-His antibody.

Protein Crystallization, Data Collection, and Structure Determination. Crystals of *Mag*KatG2 were obtained using the hanging-drop vapor-diffusion method at 4 °C with a protein concentration of 5 mg/mL in 5 mM phosphate buffer (pH 7.5). The mother liquor contained 15% PEG4000 and 0.1 M sodium acetate (pH 4.6). Prior to being flash-frozen, crystals were soaked for 5 s in a 5 mM peroxyacetic acid solution (pH 8.5) containing elevated levels of PEG4000 (35%) as a cryoprotectant. At beamline ID23-1 (ESRF, Grenoble, France), diffraction data up to 1.6 Å were obtained using a flash-cooled crystal. The crystal belonged to space group *P*2₁2₁2₁ with the following unit cell parameters: *a* = 103.6 Å, *b* = 109.6 Å, and *c* =

132.2 Å. A molecular replacement solution was found for the newly obtained data sets using the wild-type structure of *MagKatG2* [Protein Data Bank (PDB) entry 3UT2] as a search model. The protein structure was then refined at 1.60 Å resolution, giving crystallographic agreement factors R and R_{free} of 16.5 and 19.0%, respectively (Table 2). The solvent content was 47%, and a biological dimer was present in the asymmetric unit. Structure factors and coordinates have been deposited in the PDB as entry 5CJH.

UV–Vis and Electronic Circular Dichroism Spectroscopy. UV–visible spectra of wild-type *MagKatG2* and its variants were routinely recorded with a Hitachi U-3900 spectrophotometer at 25 °C. The molar absorption coefficient of the ferric, high-spin *MagKatG2* at the Soret maximum ($\epsilon_{404} = 102600 \text{ M}^{-1} \text{ cm}^{-1}$) was determined recently²⁷ and used for calculation of KatG concentrations throughout this work. The absorption coefficient of *MagKatG2* at 280 nm (ϵ_{280}) was calculated to be 147800 M⁻¹ cm⁻¹ using the protein sequence (ExPasy server). The samples were recorded in either 50 mM citrate-phosphate buffer (pH 4.0–7.0) or 50 mM phosphate buffer (pH 7.0–8.5).

Electronic circular dichroism (ECD) spectra were recorded on a Chirascan spectrophotometer (Applied Photophysics, Leatherhead, U.K.). The instrument was flushed with nitrogen with a flow rate of 5 L min⁻¹. The instrument allowed simultaneous UV–vis and ECD monitoring and was equipped with a Peltier element for temperature control. To record far-UV spectra (260–190 nm), the quartz cuvette had a path length of 1 mm, and to record visible spectra, a path length of 10 mm was used. Instrumental parameters were set as follows: spectral bandwidth, 5 nm; step size, 1 nm; scan time, 15 s per point.

To monitor thermal unfolding, 5 μM wild-type or mutant KatGs were incubated in 5 mM phosphate buffer (pH 7.0) with the temperature increasing in a stepwise manner (1 °C min⁻¹) ranging from 20 to 90 °C. Single-wavelength scans were performed with instrumental parameters set as follows: spectral bandwidth, 1 mm (Soret) or 0.5 mm (far-UV); scan time, 12 s per point. Melting temperatures (T_m) were determined by sigmoidal fitting of obtained graphs using Pro-Data Viewer software from Applied Photophysics (version 4.1.9).

Electron Paramagnetic Resonance (EPR) Spectroscopy. EPR spectroscopy was performed on a Bruker EMX continuous wave (cw) spectrometer, operating at X-band (9 GHz) frequencies. The instrument was equipped with a high-sensitivity resonator and an Oxford Instruments ESR900 helium cryostat for low-temperature measurements. Spectra were recorded under nonsaturating conditions using a microwave power of 2 mW, a modulation frequency of 100 kHz, a modulation amplitude of 1 mT, a conversion time of 41 ms, a time constant of 41 ms, and 2048 points. For the measurements, 100 μL samples of 50 μM recombinant *MagKatG2* and its variants were prepared in 50 mM citrate-phosphate buffer (pH 4.0–7.0) or 50 mM phosphate buffer (pH 7.0–8.5), transferred into Wilmad quartz tubes (3 mm inner diameter), and flash-frozen in liquid nitrogen. To remove O₂, the tubes were flushed with argon while the sample was kept frozen on dry ice. Measurements were performed at 10 K.

Catalatic Activity Measurements. Apparent kinetic parameters of catalase activity were determined polarographically using a Clark-type electrode from Hansatech (Oxygraph plus). The temperature was held constant at 30 °C by a thermostat-controlled water bath. The electrode was

equilibrated by flushing the stirred reaction chamber with either dioxygen (O₂) (100% saturation) or pure nitrogen (N₂) (0% saturation). Reactions were started in oxygen-free 50 mM citrate-phosphate (pH 4.0–7.0) or 50 mM phosphate buffer (pH 7.0–8.5) by addition of enzyme.

Peroxidatic Activity Measurements. Peroxidatic activity was monitored spectrophotometrically by using 1 mM peroxyacetic acid and ABTS or guaiacol as one-electron donors (1 mM) (all from SigmaAldrich). One unit of peroxidase was defined as the amount of enzyme that oxidizes 1 μmol of selected electron donor per minute at the pH optimum and 25 °C.

Stopped-Flow Spectroscopy. Kinetic measurements of the direct reaction between the ferric proteins with cyanide, hydrogen peroxide, and peroxyacetic acid at 25 °C were performed using SX-18MV or Pi*-180 stopped-flow machines from Applied Photophysics. The path length of the optical cells was 10 mm and the volume 20 μL. Peroxide solutions were prepared freshly and diluted in appropriate 50 mM citrate-phosphate buffer (pH 4.0–7.0) or 50 mM phosphate buffer (pH 7.0–8.5).

Calculation of pseudo-first-order rate constants (k_{obs}) was performed with the Pro-Data Viewer software (Applied Photophysics, version 4.1.9). Second-order rate constants were determined from plots of k_{obs} versus substrate concentration.

Differential Scanning Calorimetry. Thermal denaturation of *MagKatG2* and its variants was monitored using a VP-DSC MicroCal LLC calorimeter from GE Healthcare. The machine uses a cell volume of 137 μL and is equipped with a cooled autosampler for 96-well plates and automated cell cleaning and sample injection. The protein concentration of all samples was 5 μM in 5 mM phosphate buffer (pH 7.0). The differential heat capacity (ΔC_p) was recorded between 20 and 90 °C with a heat rate of 60 °C h⁻¹. Baseline correction of the recorded thermograms was done by subtraction of buffer runs or rescans of each respective sample. After normalization for the exact protein concentrations, the acquired peaks were fitted by a non-two-state unfolding model using the LLC-Cap-DSC add-on of Origin 7.0 software (OriginLab).

Molecular Dynamics Simulations. Molecular dynamics simulations of a monomer of *MagKatG2* were performed to study the effect of the Tyr273Phe mutation on the structure and dynamics of the protein. The crystal structure of *MagKatG2* at 1.55 Å resolution with PDB entry 3UT2 served as a starting point with clearly defined electron density maps for main and side chains of residues Thr51–Val782.⁸ Because of its flexibility, the structure of the N-terminal part of the protein could not be determined. Also note that the simulation, which was performed with only the monomer, does not include the intersubunit disulfide bridge of the native dimeric protein. For simulation, the N- and C-termini were charged, all arginines, cysteines, and lysines were protonated, and all aspartates and glutamates were deprotonated. In wild-type *MagKatG2*, the side chains of Trp140 (C γ 2) and Tyr273 (C ϵ 1) as well as Tyr273 (C ϵ 2) and Met299 (S δ) were covalently connected to form the KatG-typical adduct. Mobile Arg412 in the “in” position (pointing to Tyr273 or Phe273) was used. All histidines were protonated at N δ . The heme group was modeled in the ferric state, and its iron atom was covalently tethered to N ϵ of His314. From this “wild-type” structure, a second structure with the Tyr273Phe mutation was prepared,

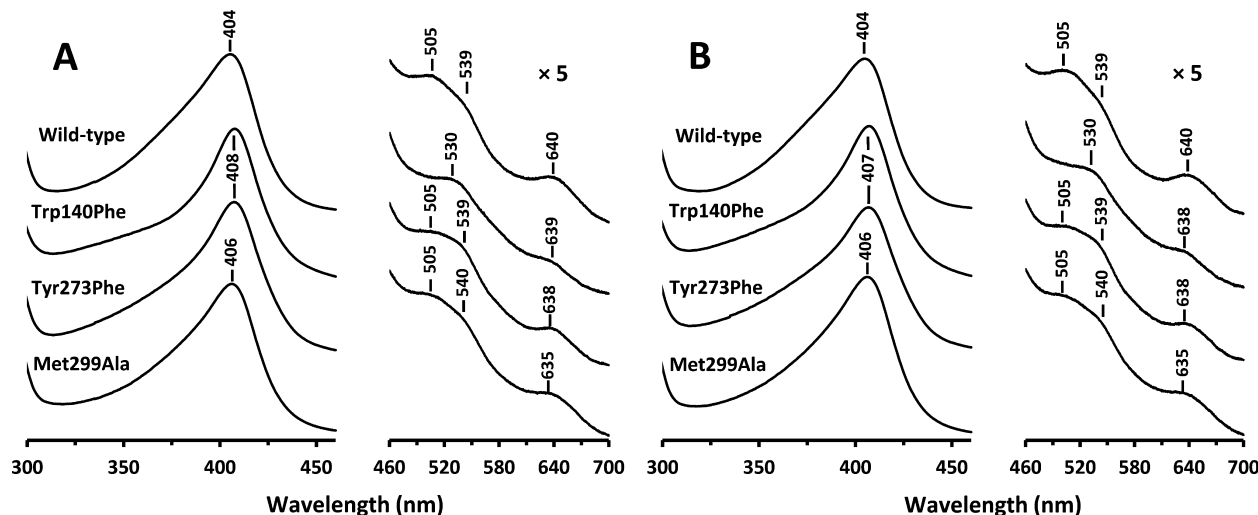


Figure 1. UV-vis spectra of wild-type MagKatG2 and the three adduct variants Trp140Phe, Tyr273Phe, and Met299Ala. Conditions: 7 μ M protein in (A) 50 mM citrate-phosphate buffer (pH 5.5) and (B) 50 mM phosphate buffer (pH 7.0). The wavelength range between 460 and 700 nm is expanded by a factor of 5 for better visibility.

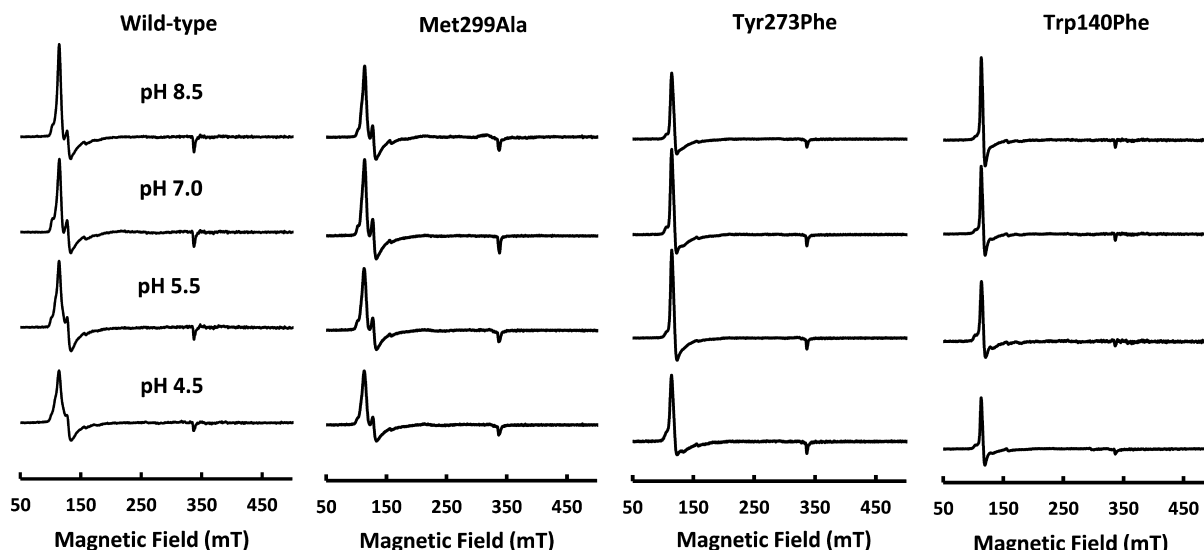


Figure 2. Low-temperature cw EPR spectra of wild-type MagKatG2 and the adduct variants Trp140Phe, Tyr273Phe, and Met299Ala. Conditions: 50 μ M protein in 50 mM citrate-phosphate buffer (pH 4.5 or 5.5) or 50 mM phosphate buffer (pH 7.0 or 8.5).

in which amino acids Trp140, Phe273, and Met299 were not covalently tethered to each other.

All MD simulations were conducted employing the GROMOS11 software package²⁹ with the S4A7 force field.³⁰ The two studied systems were energy-minimized *in vacuo* using the steepest-descent algorithm. Energy-minimized systems were placed into a periodic, pre-equilibrated, and rectangular box of SPC water.³¹ Minimum solute to box wall and minimum solute to solvent distances were set to 0.8 and 0.23 nm, respectively. To relax unfavorable atom–atom contacts between the solute and the solvent, energy minimization of the solvent was performed while keeping the solute positionally restrained using the steepest-descent algorithm. Finally, 43 water molecules that had the most favorable electrostatic potential for replacement with a positive or negative ion were replaced with 30 sodium and 13 chloride ions, respectively, to achieve electroneutrality in both systems and to account for the ionic strength present during experimental procedures. After these procedures, system “wild-type” contained 7314 protein atoms,

43 ions, and 67053 water atoms, whereas system “Tyr273Phe” contained 7316 protein atoms, 43 ions, and 66537 water atoms. For equilibration, the following protocol was used. Initial velocities were randomly assigned according to a Maxwell–Boltzmann distribution at 50 K. All solute atoms were positionally restrained through a harmonic potential with a force constant of 2.5×10^4 kJ mol⁻¹ nm⁻² not to disrupt the initial conformation, and the systems were propagated for 20 ps. In each of the five subsequent 20 ps MD simulations, the positional restraints were reduced by 1 order of magnitude and the temperature was increased by 50 K.

After equilibration, production runs with roto-translational constraints on all solute atoms³² were conducted for 50 ns at constant temperature (300 K) and pressure (1 atm). Temperature and pressure were kept constant using the weak-coupling scheme³³ with coupling times of 0.1 and 0.5 ps, respectively. The isothermal compressibility was set to 4.575×10^{-4} kJ⁻¹ mol nm³, and two separate temperature baths were used for solute and solvent. The SHAKE algorithm was used to

constrain bond lengths,³⁴ allowing for 2 fs time steps. Nonbonded interactions were calculated using a triple-range scheme. Interactions within a short-range cutoff of 0.8 nm were calculated at every time step from a pairlist that was updated every fifth step. At these points, interactions between 0.8 and 1.4 nm were also calculated explicitly and kept constant between updates. A reaction field³⁵ contribution was added to the electrostatic interactions and forces to account for a homogeneous medium outside the long-range cutoff using a relative dielectric constant of 61 as appropriate for the SPC water model.³⁶ Coordinate and energy trajectories were stored every 0.5 ps for subsequent analysis. A clustering analysis on the large loop 1 conformations was performed on a subset of 10000 protein structures separated by 5 ps. For this, the root-mean-square deviations (rmsds) for the loop backbone atoms after a roto-translational fit of the entire protein were calculated for all pairs of structures and clustering was performed using a greedy algorithm³⁷ with a similarity cutoff of 0.15 nm.

RESULTS

Spectral Features of Wild-Type MagKatG2 and Mutants with the Disrupted Trp-Tyr-Met Adduct. The UV-vis spectrum of recombinant dimeric MagKatG2 (monomer size of 85 kDa) showed all bands typical for a heme *b* containing peroxidase in the high-spin ferric state with a Soret maximum at 404 nm, Q-bands at 505 and 539 nm, and a broad CT1 band at 640 nm (Figure 1). The Reinheitszahl (purity number, A_{404}/A_{280}) varied between 0.65 and 0.69. The protein was stable in the pH range from 4.5 to 8.5, giving rise to almost identical UV-vis and EPR spectra (Figures 1 and 2). The EPR spectrum does not give evidence of hexacoordinated low-spin heme but represents a mixture of high-spin heme forms of differently pronounced rhombicity (Figure 2).

Upon disruption of the KatG-typical covalent adduct by site-directed mutagenesis, the absorbance maxima of the mutants were slightly red-shifted but still reflected the presence of high-spin ferric states. Figure 1 compares the spectra of wild-type MagKatG2 at pH 5.5 and 7.0 with those spectra of the three variants, Trp140Phe, Tyr273Phe, and Met299Ala, recorded under the same conditions. The purity numbers of the three recombinant mutant proteins varied from one preparation to another and were in the ranges of 0.62–0.70 for Trp140Phe, 0.58–0.65 for Tyr273Phe, and 0.55–0.66 for Met299Ala. Comparison of panels A and B of Figure 1 clearly demonstrates almost identical UV-vis spectral signatures of the three mutant proteins at pH 7.0 and 5.5. Far-UV-vis electronic circular dichroism spectra (260–190 nm) of wild-type MagKatG2 and the three mutants were identical at pH 7.0 (Supplemental Figure 1) and pH 5.5 (data not shown), clearly suggesting identical secondary structure composition in the four proteins.

Figure 2 compares representative cw low-temperature EPR spectra as a sum of individual high-spin species. The obtained EPR spectra indicate very similar heme geometry with low rhombicity in wild-type MagKatG2 and the mutant Met299Ala within the pH range of 4.5–8.5. By contrast, the spectra of both Tyr273Phe and Trp140Phe were slightly different, represented by a shift to axial site geometry.

Role of the Trp-Tyr-Met Adduct in the Overall Structure and Thermal Stability. Despite the very small impact of manipulation of the Trp-Tyr-Met adduct on spectral signatures, active site geometry, and overall structure, its disruption dramatically decreased the thermal stability of this fungal catalase-peroxidase. At room temperature, all four

proteins were dimeric in solution and showed a single band at ~85 kDa (the theoretical molar mass of the monomer plus a heme and a His₆ tag is 85.30 kDa) in sodium dodecyl sulfate–polyacrylamide gel electrophoresis under reducing conditions. Under nonreducing conditions, one band at 170 kDa was observed for both the wild-type and mutant proteins, indicating the presence of dimers only. This suggests that engineering of the Trp-Tyr-Met adduct had no impact on the formation of the interchain disulfide bridges between Cys55 and Cys74 of the N-terminal domains. These cystine bridges are found in only secreted eukaryotic KatGs, not in intracellular eukaryotic or prokaryotic counterparts.⁸ Figure 3 compares the temperature-

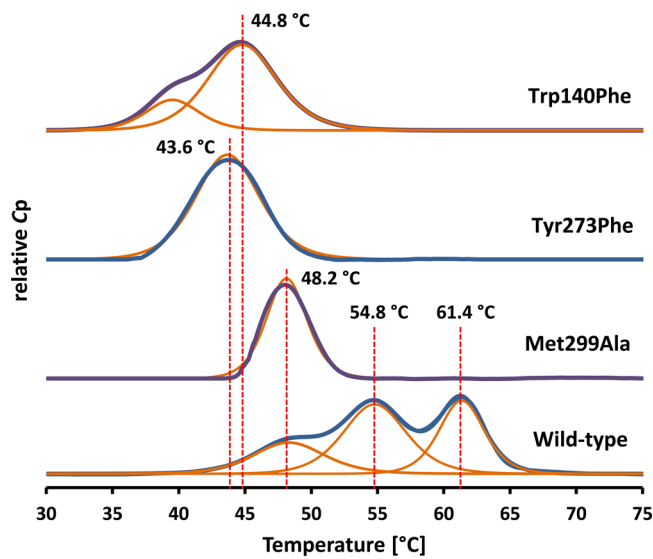


Figure 3. Thermal stability of wild-type MagKatG2 and variants Trp140Phe, Tyr273Phe, and Met299Ala. Differential scanning calorimetric measurements were performed with 5 μ M protein in 5 mM phosphate buffer (pH 7.0) using a heating rate of 60 $^{\circ}$ C h⁻¹. The obtained baseline-corrected thermograms are shown as bold blue lines, and the corresponding fitted non-two-state transition peaks are depicted as thin orange lines. Dashed vertical lines have been inserted for the presentation of respective melting temperatures.

mediated unfolding pathways of the four proteins followed by differential scanning calorimetry (DSC). Comparison of the four thermograms demonstrates the importance of the adduct in the maintenance of the thermal stability of MagKatG2. The wild-type protein follows a non-two-state unfolding with two main transitions at 54.8 and 61.4 $^{\circ}$ C. An additional minor transition with a T_m value of 48.2 $^{\circ}$ C was observed, but the area under this peak slightly changed depending on the protein batch. Upon exchange of Met299, the thermal stability was significantly reduced and only one endothermic peak occurred. In both Trp140Phe and Tyr273Phe, the thermal stability was even more decreased (Figure 3).

Additionally, temperature-mediated unfolding was followed by monitoring the decrease in ellipticity at 208 nm [which represents the typical minimum of a protein composed of mainly α -helical structure (see the insets of Supplemental Figure 1)]. Supplemental Figure 1 compares the (very similar) unfolding curves of the three variants fitted by assumption of a two-state transition with calculated T_m values of 45 $^{\circ}$ C (Met299Ala) and 44 $^{\circ}$ C (Tyr273Phe and Trp140Phe). By contrast, unfolding of wild-type MagKatG2 suggests the

presence of an intermediate state with calculated T_m values of 52 and 58 °C.

Because KatGs contain (noncovalently bound) heme *b*, we also followed the release of the prosthetic group from the protein during unfolding. In these experiments, the loss of heme ellipticity at 412 nm (wild-type *MagKatG2*) and 410 nm (variants) was followed. In the case of the three mutant proteins, the release of the prosthetic group occurred simultaneously with the loss of secondary structure (not shown). With wild-type *MagKatG2*, loss of heme ellipticity started above 45 °C and more than 80% was lost between 52 and 60 °C. This suggests that the second transition seen in **Supplemental Figure 1** of wild-type *MagKatG2* represents unfolding of the more stable N-terminal heme-containing domain.

It has to be mentioned that within this project we have also tried to determine the crystal structures of the three mutant proteins. Because *MagKatG2* is much more stable than its prokaryotic counterparts,⁸ we hoped to grow well-diffracting crystals of relevant adduct mutants. However, most probably because of the important role this posttranslational modification plays in protein stability and dynamics (see below), crystallization trials failed.

Catalytic Activity of *MagKatG2* and Adduct Variants: Steady-State Kinetics and Spectral Features of Redox Intermediates. Next we probed the impact of adduct engineering on the *catalytic* activity by monitoring the release of dioxygen with a Clark-type electrode. **Table 1** summarizes the data of these kinetic investigations. *MagKatG2* exhibits an overwhelming catalase activity with a turnover number (k_{cat}) of 6450 s⁻¹ at the pH optimum (pH 5.25) and an apparent K_M value of 3.84 mM. With increasing pH, k_{cat} values decreased, being 51% at pH 7.0 and 11.8% at pH 8.0. The apparent K_M values slightly decreased with increasing pH.

Upon disruption of the covalent Trp-Tyr-Met adduct by site-directed mutagenesis, the catalase activity was drastically reduced. Whereas the pH optima of the three variants, Trp140Phe, Tyr273Phe, and Met299Ala, were still within the pH range of 5.2–5.5, the absolute k_{cat} values at the pH optimum were 2.1% (Trp140Phe), 0.8% (Tyr273Phe), and 3.1% (Met299Ala) of that of the wild-type enzyme (**Table 1**). Additionally, the apparent K_M values decreased by 75–83% (**Table 1**). In contrast to the *catalytic* activity, the respective variants showed wild-type-like (Trp140Phe and Tyr273Phe) or even higher (Met299Ala, 165–270%) specific peroxidase activities at pH 6.5 with either ABTS (100%, 17.2 units/mg) or guaiacol (100%, 1.1 units/mg) in the presence of peroxyacetic acid. These data clearly underline that similar to prokaryotic KatGs the Met-Tyr-Trp adduct, in its entirety, is essential for the catalase but not for the peroxidase activity of eukaryotic KatGs.

Furthermore, we elucidated the spectral signatures of the redox intermediate of *MagKatG2* that dominates during H₂O₂ degradation. Upon reaction of 3.5 μM ferric *MagKatG2* with 10 mM H₂O₂ within 1.0 ms, a low-spin species was formed. In the pH range of 6.5–9.0, this species was characterized by a red-shifted Soret band, hyperchromicity in the Q-band region (505 and 539 nm), formation of a broad shoulder around 520 nm, and disappearance of the high-spin CT at 640 nm (**Figure 4A**). This reaction intermediate dominated and was present until H₂O₂ had been totally depleted (inset of **Figure 4A**).

Under more acidic conditions (pH ≤ 6.0), the spectral signatures of the dominating redox intermediate of *MagKatG2*

Table 1. Comparison of Apparent Catalytic Parameters of Hydrogen Peroxide Dismutant Activity of Eukaryotic Secreted Wild-Type and Mutated Catalase-Peroxidase from *MagKatG2*^a

	k_{cat} (s ⁻¹)	K_M (mM)	k_{cat}/K_M (M ⁻¹ s ⁻¹)	ref
<i>MagKatG2</i>				
wild type at pH 7.0	3290 ± 251	2.77 ± 0.66	(1.2 ± 0.3) × 10 ⁶	27
wild type at pH 5.25	6450 ± 187	3.84 ± 0.23	(1.7 ± 0.2) × 10 ⁶	27
W140F	135 ± 2	0.97 ± 0.06	(1.4 ± 0.1) × 10 ⁵	this work
Y273F	49 ± 3	0.64 ± 0.23	(7.7 ± 3.1) × 10 ⁴	this work
M299A	199 ± 7	0.91 ± 0.17	(2.2 ± 0.4) × 10 ⁵	this work
<i>SynKatG</i>				
wild type	7630	3.1	2.5 × 10 ⁶	50
W122F	ND ^b	ND ^b	ND ^b	
Y249F	6	4.9	1.2 × 10 ³	4
M275I	20	5.8	3.4 × 10 ³	15
<i>MtKatG</i>				
wild type	4350	2.4	1.8 × 10 ⁶	50
W107F	/	/	/	
Y229F	—	—	4.0 × 10 ²	17
M255I	1	40.2	2.7 × 10	13
<i>BpKatG</i>				
wild type	5680	4.5	1.3 × 10 ⁶	50
W111F	2	—	—	51
Y238F	6	—	—	51
M264A	6	—	—	51

^aIn activity measurements, the release of O₂ was followed polarographically at the activity optimum of pH 5.25 using a Clark-type electrode. For wild-type *MagKatG2*, the apparent kinetic parameters are also given for pH 7.0. Reaction conditions: 50 mM citrate-phosphate buffer (pH 5.25) or 50 mM phosphate buffer (pH 7.0) and 30 °C. For comparison, literature data about apparent kinetic constants (pH 7.0) of prokaryotic catalase-peroxidases are provided.

^bNot detectable.

during turnover were different. **Figure 4B** shows the reaction between 3.5 μM wild-type *MagKatG2* and 10 mM H₂O₂ at pH 5.25. The reaction was extremely fast, and within 500 ms, H₂O₂ was fully degraded (inset of **Figure 4B**). After the reactants had been mixed in the stopped-flow apparatus, the Soret band was immediately red-shifted and two additional peaks with maxima around 545 and 580 nm appeared, whereas the CT band at 640 nm disappeared. This spectrum (dashed line in **Figure 4B**) was reminiscent of the corresponding spectrum obtained from prokaryotic KatGs under similar reaction conditions as described by Jakopitsch et al.¹⁶ The kinetics of depletion of this redox intermediate roughly followed the rapid kinetics of hydrogen peroxide degradation as depicted in the inset of **Figure 4B**.

In all cases, the appearance and life span of the respective reaction intermediate that dominated during hydrogen peroxide degradation were directly related to the amount of peroxide and the pH dependence of the *catalytic* activity observed in the polarographic steady-state measurements. **Figure 4C** compares time traces derived from stopped-flow experiments (conditions as in **Figure 4A,B**) that studied the degradation of 2 and 10 mM H₂O₂ at 240 nm. At its pH optimum, 3.5 μM *MagKatG2* was able to completely dismutate 10 mM H₂O₂ within <0.5 s, whereas at pH 8.5, it took almost 8 s to completely degrade

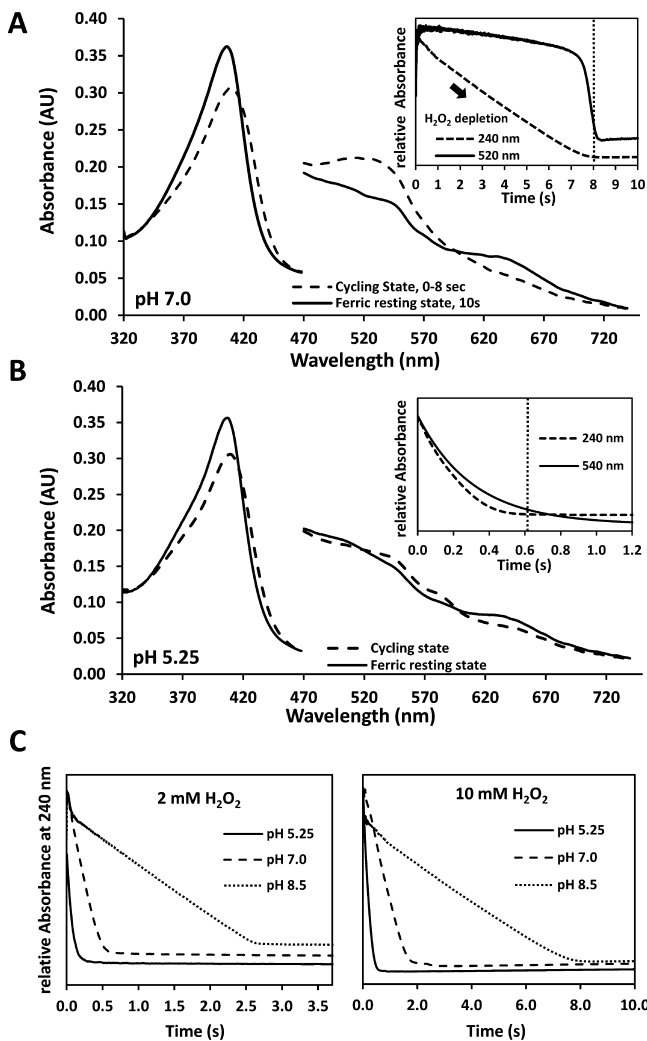


Figure 4. Reaction of wild-type MagKatG2 with hydrogen peroxide at pH 7.0 and 5.25. Conventional stopped-flow spectroscopy was used for mixing of 7 μ M MagKatG2 with a 2850-fold molar excess of hydrogen peroxide. Spectra were recorded 1 ms (up to 10 s) after mixing. Final conditions: 3.5 μ M MagKatG2 and 10 mM H₂O₂ in 50 mM phosphate buffer (pH 7.0) (A) or 50 mM phosphate-citrate buffer (pH 5.25) (B). The insets show time traces at 240 nm (monitoring degradation of H₂O₂) and 520 nm (pH 7.0) or 540 nm (pH 5.25) (monitoring the decay of the dominating enzyme intermediate during turnover). (C) Concentration and pH-dependent depletion of 2 and 10 mM hydrogen peroxide by wild-type MagKatG2. Conditions: 3.5 μ M MagKatG2 in 50 mM phosphate buffer (pH 7.0 or 8.5) or 50 mM phosphate-citrate buffer (pH 5.25).

hydrogen peroxide (Figure 4C). Neither at pH 5.25 nor under basic pH conditions was there evidence of inhibition of MagKatG2 by H₂O₂ (at least up to the tested H₂O₂/MagKatG2 molar ratio of ~3000).

As already outlined above, disruption of the covalent adduct by mutagenesis converts a bifunctional MagKatG2 into a typical monofunctional peroxidase. Together with the dramatic loss of catalytic activity (Table 1), when variants Trp140Phe, Tyr273Phe, and Met299Ala were mixed with H₂O₂, redox intermediates with completely different spectral features were observed. Typically, they resembled those intermediates formed by mixing (monofunctional) peroxidases of the peroxidase-catalase superfamily with H₂O₂ in the absence of exogenous electron donors.³⁸ Figure 5A shows the consecutive inter-

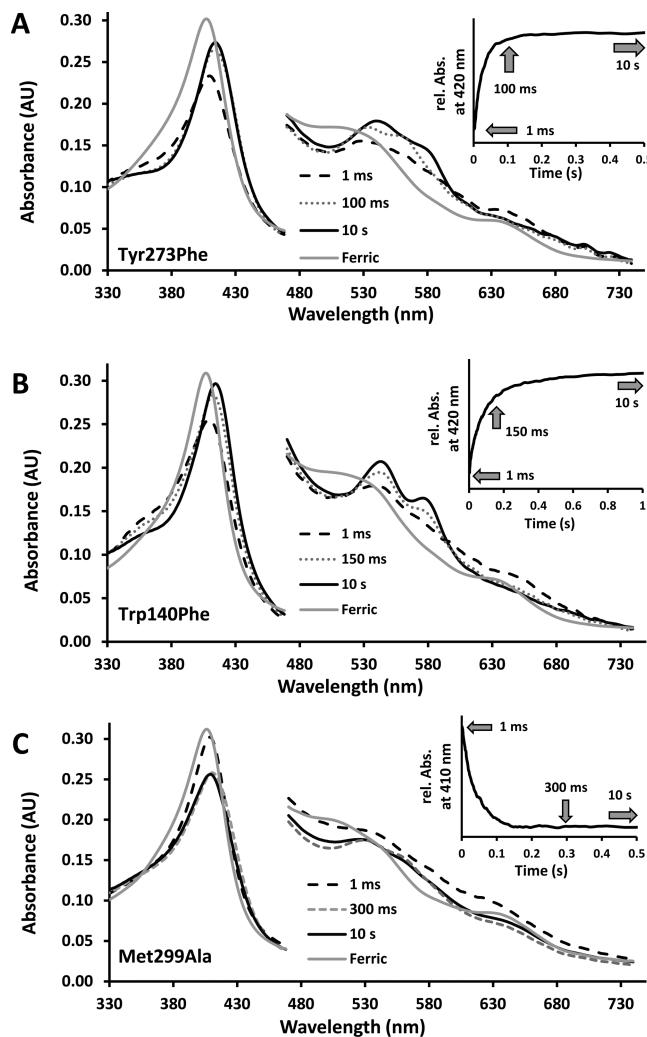


Figure 5. Reaction of ferric MagKatG2 adduct variants Tyr273Phe (A), Trp140Phe (B), and Met299Ala (C) with hydrogen peroxide. Spectra of ferric proteins are colored gray, and the first spectrum collected 1.0 ms after mixing with H₂O₂ is shown as a dashed black line. Intermediate spectra and final spectra are shown as gray dotted lines and black lines, respectively. Insets show time traces at 420 nm for Tyr273Phe and Trp140Phe and 410 nm for Met299Ala. Arrows in the inset indicate the point of time of selection of spectra. Final conditions: 3 μ M protein in 50 mM phosphate buffer (pH 7.0) and excess of hydrogen peroxide (1000-fold for panel A, 50-fold for panel B, and 10-fold for panel C). For Tyr273Phe (A) and Trp140Phe (B), the first collected spectrum (dashed line) represents that of Compound I, which converts to a Compound III-like state (black line) within 10 s. With Tyr273Phe, a spectrum representing a Compound II-like intermediate state could be trapped (dotted line). Assignment of spectral features of Met299Ala to distinct redox intermediates is too vague (see the text).

conversion of ferric Tyr273Phe (gray line) to Compound I (dashed black line; hypochromicity at the Soret maximum), followed by a Compound II-like species (dotted gray line; 416, 530, and 558 nm) leading to a Compound III-like species (black line; 418, 542, and 576 nm) at the end of the series. Figure 5B follows the interconversion of ferric Trp140Phe (gray line) to Compound I (dashed black line; hypochromicity at the Soret maximum), followed by immediate formation of a Compound III-like species (dotted gray and black line; 416, 542, and 576 nm). Spectra are shown for pH 7.0, and very similar spectra were observed at pH 5.5 and 8.5 (not shown).

Besides lacking Compound II-like species for the Trp140Phe variant, the two mutant proteins differ in the kinetics of interconversion of ferric enzyme → Compound I → Compound II-like species (Tyr273Phe only) → Compound III-like species as demonstrated in the insets of Figure 5 for the reactions at pH 7.0. With Tyr273Phe, the interconversion of the redox intermediates mediated by H_2O_2 was very fast. Upon addition of H_2O_2 to Met299Ala, both the hypochromicity at the Soret maximum (reflecting Compound I formation) and its accompanying red-shift were less pronounced. The final spectrum observed 10 s after mixing was a mixture of Compound II-like and Compound III-like species.

Probing the Accessibility of the Ligand and Peroxide to the Active Site of Wild-Type and Mutant MagKatG2. Besides the Trp-Tyr-Met adduct, the presence of large loop insertions distinguishes KatGs from its related monofunctional peroxidases of Class 1 of the peroxidase-catalase superfamily.³⁸ These loops contribute to the architecture of the long and restricted access channel that leads from the molecular surface of the protein to the deeply buried heme cavity.^{22,39} Moreover, large loop 1 (LL1), found in the proximity of the active site, is anchored via Tyr273 at the covalent adduct in the wild-type protein (see also Figure 7A). Thus, it is reasonable to assume that elimination of its anchor might have an impact on ligand or substrate accessibility and binding.

First, we probed the kinetics of binding of cyanide to the heme group of wild-type and mutant proteins. Upon binding of cyanide, the low-spin cyanide complex of MagKatG2 that is characterized by a red-shifted Soret band (418 nm) and two characteristic peaks at 525 and 540 nm is formed. The UV-vis spectra of the cyanide complexes of the three adduct variants were very similar (Supplemental Figure 2) as were the binding rates $\{[Trp140Phe, (1.8 \pm 0.2) \times 10^5 M^{-1} s^{-1}] < [Met299Ala, (2.4 \pm 0.2) \times 10^5 M^{-1} s^{-1}] < [wild-type MagKatG2, (5.4 \pm 0.2) \times 10^5 M^{-1} s^{-1}] < [Tyr273Phe, (9.2 \pm 0.3) \times 10^5 M^{-1} s^{-1}]\}$ (Supplemental Figure 2). Similarly, there was only a small variability in k_{off} values ranging from $1.5 s^{-1}$ (wild-type MagKatG2) to $4.3 s^{-1}$ (Tyr273Phe) and thus in calculated K_d values ($=k_{off}/k_{on}$) (wild-type MagKatG2, $14.4 \mu M$; Trp140Phe, $12.3 \mu M$; Tyr273Phe, $4.6 \mu M$; Met299Ala, $17.4 \mu M$).

Next we evaluated the effect of elimination of the adduct on the kinetics of oxidation of the ferric proteins by peroxyacetic acid (PAA). Oxidation of wild-type MagKatG2 with PAA follows a monophasic reaction with an apparent bimolecular rate constant of $(7.51 \pm 0.15) \times 10^3 M^{-1} s^{-1}$ at pH 7.0. At pH 5.0 and 8.5, the respective rates were decreased by 12 and 57%, respectively. The reaction was accompanied by a hypochromicity in the Soret region, formation of a peak at 542 nm and of two broad absorbances around 596 and 645 nm (Figure 6A) suggesting the formation of Compound I [oxoiron(IV)-porphyrin cation radical species].⁴⁰ In the absence of exogenous electron donors, Compound I slowly decays to the ferric resting state (not shown), including migration of the porphyrin cation radical toward the protein as demonstrated for prokaryotic KatGs.⁴⁰ The transiently formed oxoiron intermediate represents an alternative structure of Compound I (often designated as Compound I*).

Importantly, upon disruption of the covalent Trp-Tyr-Met adduct, the rate of oxidation of the mutant proteins by PAA was significantly increased. The reactions were biphasic with a rapid reaction being responsible for ~90% of the absorbance change at the Soret maximum followed by a slow linear phase. Single-exponential fitting of the rapid phase allowed calculation of k_{obs}

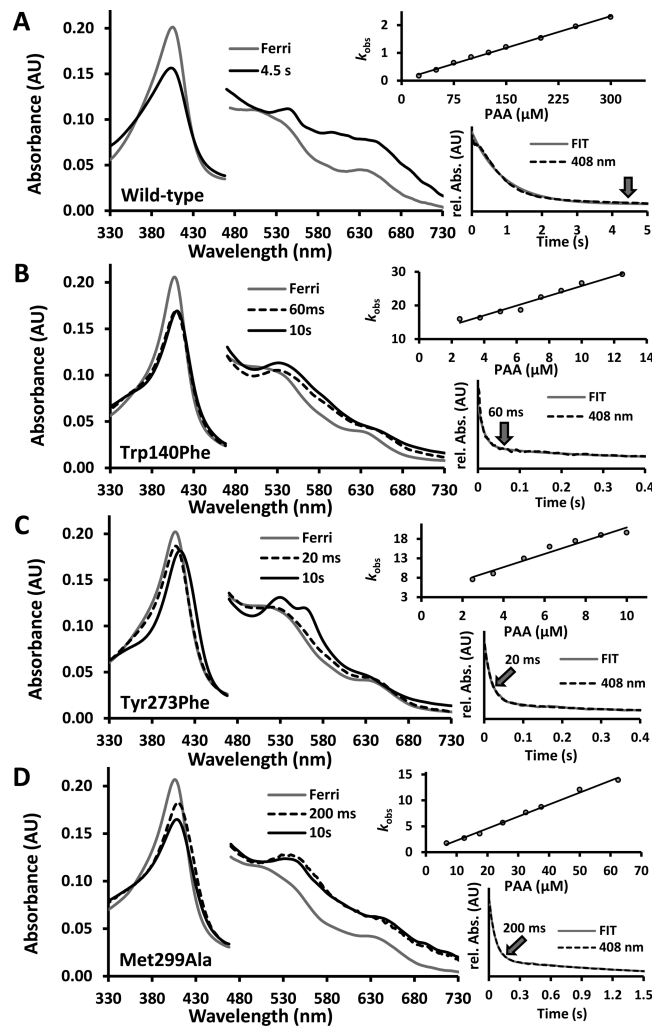


Figure 6. Reaction of ferric wild-type MagKatG2 and the adduct variants Trp140Phe, Tyr273Phe, and Met299Ala with peroxyacetic acid (PAA). Gray lines indicate the ferric resting state, dashed black lines the intermediate present shortly after mixing, and black lines the spectral features of the intermediate selected 10 s after mixing. Additionally, typical time traces at 408 nm of the respective proteins are shown together with a single-exponential fit for the first fast phase of the reaction used for the secondary plots (k_{obs} vs PAA concentration). Arrows indicate the time points of selection of the Compound I spectrum. Conditions: $2 \mu M$ protein in 50 mM phosphate buffer (pH 7.0). (A) Wild-type MagKatG2 and $300 \mu M$ PAA. (B) Trp140Phe and $70 \mu M$ PAA. (C) Tyr273Phe and $20 \mu M$ PAA. (D) Met299Ala and $120 \mu M$ PAA.

values that were linearly dependent on the PAA concentration. Calculation of apparent rate constants at pH 7.0 showed the following hierarchy: Trp140Phe $\{[1.46 \pm 0.11] \times 10^5 M^{-1} s^{-1}] < [Met299Ala, (2.32 \pm 0.08) \times 10^5 M^{-1} s^{-1}] < [Tyr273Phe, (1.70 \pm 0.17) \times 10^6 M^{-1} s^{-1}]\}$ (insets of Figure 6). Upon oxidation of Trp140Phe to Compound I (first rapid phase), the Soret absorbance decreased and two bands at 530 and 645 nm were observed after 60 ms that finally shifted to 532 and 650 nm, respectively, after incubation for 10 s (Figure 6B). Upon oxidation of Tyr273Phe, the absorbance of the rapidly formed species (20 ms) slightly decreased in the Soret region and showed peaks at 407, 522, and 635 nm. After incubation for 10 s, the resulting intermediate had its Soret absorbance at 412 nm and two clear peaks at 530 and 560 nm, as well as a shoulder at

632 nm (Figure 6C). The consecutively formed oxidized species of Met299Ala showed spectral bands at 410, 532, and 632 nm (200 ms) and finally, after incubation for 10 s, at 408, 530, and 635 nm, respectively (Figure 6D).

X-ray Structure of an Oxoiron Compound of MagKatG2. Next, we soaked crystals of MagKatG2 with PAA for 5 s prior to flash-freezing them and succeeded in determining the crystal structure at 1.60 Å resolution (Table 2)

Table 2. Data Collection and Structural Refinement Statistics for MagKatG2 Soaked with PAA

Data Collection	
space group	P2 ₁ 2 ₁ 2 ₁
unit cell parameters <i>a</i> , <i>b</i> , <i>c</i> (Å)	103.6, 109.6, 132.2
resolution (Å)	30–1.60 (1.64–1.60)
no. of unique reflections	196582 (14410)
completeness (%)	99.5 (99.3)
<i>R</i> _{syn} (%)	8.7 (64.6)
<i>R</i> _{meas} (%)	9.9 (73.3)
$\langle I/\sigma I \rangle$	11.2 (2.4)
redundancy	4.5 (4.6)
Model Refinement	
resolution (Å)	20–1.6 (1.64–1.60)
no. of reflections	186717 (13557)
no. of free reflections	9850 (759)
<i>R</i> _{cryst} (%)	16.5 (25.9)
<i>R</i> _{free} (%)	19.0 (29.0)
no. of residues	1467
no. of waters	1573
no. of ligands	2
average <i>B</i> factor (Å ²)	
protein	17.6
ligands	17.1
water	26.1
all atoms	18.6
rmsd	
bond lengths (Å)	8 × 10 ⁻³
bond angles (deg)	1.39

and Figure 7). The overall structure remained unchanged compared to that of the native (nominally) ferric enzyme (PDB entry 3UT2),⁸ but the electron density maps showed several differences in the vicinity of the heme. The continuous density extending from the heme iron to a second atom is best explained by formation of an oxoiron species with an iron–oxygen distance of 2.0 Å. This is comparable with a distance of 1.89 Å measured in the structure (at 2.2 Å resolution) of prokaryotic KatG from *Burkholderia pseudomallei* (*BpKatG*) oxidized by PAA.⁴¹ This iron–oxygen distance is considerably longer than the values measured for Compound I of cytochrome *c* peroxidase (CcP) (1.63 Å, obtained using a multicrystal processing approach) and of ascorbate peroxidase (APX) (1.73 Å, obtained upon photoreduction of the ferrous-oxy species Compound III).⁴¹ In both CcP and APX, reduction of Compound I is accompanied by lengthening of the Fe–O bond and likely protonation of the oxygen.⁴² Thus, it is reasonable to assume that the MagKatG2 structure obtained by soaking with PAA represents a Compound I* formed by either migration of the porphyrin cation radical or photoreduction of Compound I, accompanied by protonation of the ferryl oxygen. Distances between the oxo oxygen and the nitrogens from the

indole ring of Trp140 and from the imidazole ring of the distal His141 are 3.0 and 3.3 Å, respectively (Figure 7C).

Electron density also indicates that the heme vinyl group of pyrrole ring I is modified in the oxidized MagKatG2 structure, with the modification placed mainly at the proximal side of the heme (Figure 7B,C). A modification like this has never been reported for any KatG structure. However, the vinyl group was modified as well in the first reported *BpKatG* structure determined,⁶ though the modification was placed only on the distal side of the heme. Therefore, it appears that in KatGs the heme group itself can react, at least transiently, with reactive substrates or catalytic intermediates and that the heme proximal side is somehow more accessible in MagKatG2. Another difference between the native and oxidized MagKatG2 structures concerns the modification (by two oxygen atoms) at the indole nitrogen of Trp140, which is present in the native but not in the oxidized form. The side chain of the mobile Arg461, which is known to adopt two conformations in the ferric state depending on pH,⁴¹ namely “in” (ionic interaction with Tyr273 of the adduct) or “out” (well removed from the heme), shows exclusively the “out” conformation in the oxidized form, similar to what was found for the corresponding structure of *BpKatG*.

Molecular Dynamics Simulations of Ferric MagKatG2 and Mutant Tyr273Phe. It has been demonstrated above that the integrity of the covalent adduct is very important for the thermal stability of MagKatG2. Additionally, upon disruption of the adduct, the formation of the low-spin cyanide complex and, above all, the oxidation of the ferric enzyme by peroxyacetic acid were significantly enhanced. Because Tyr273 is the anchor of LL1 that contributes to the architecture of the main access channel (Figure 7A), we hypothesized that disruption of the adduct decreases its rigidity, thereby increasing flexibility and accessibility to the active site. To gain more insight into the role of Tyr273 in protein stability, 50 ns molecular dynamics (MD) simulations of the monomeric form in water of both wild-type MagKatG2 and variant Tyr273Phe were performed at pH 7.0 (started with Arg461 in the “in” conformation). Figure 8 demonstrates that the atom positional root-mean-square fluctuations (rmsfs) are significantly increased in the mutant protein. This is seen by comparison of the rmsf values of both the N-terminal and C-terminal domains of the monomeric proteins, considering either the whole protein (Figure 8A) or the backbone atoms (Figure 8B) and zooming in on residues 228–279 of LL1 only (Figure 8C). The rmsf values of the adduct itself are given in Figure 8D. The fluctuations of Trp140 are virtually unchanged, most probably because of π-stacking of this residue to the heme cofactor. The corresponding values for Phe273 and Met299 are significantly increased in Tyr273Phe compared to those of wild-type MagKatG2. Supplemental Figure 3 compares the atom-positional rmsds with respect to the initial structure of wild-type MagKatG2 and the Tyr273Phe variant as a function of simulation time. Larger deviations for the variant are clearly observed, which is also reflected by a comparison of the initial and final structures of the simulations in Supplemental Figure 4. These observations reflect the spectroscopic studies in this work as well as those published for prokaryotic KatGs that clearly demonstrated similar spectral features in ferric wild-type proteins and variants with intact Trp but exchanged Tyr.

It has to be mentioned that in the monomeric model protein used for MD simulations the N-terminus is highly flexible because of the absence of the second subunit and of the

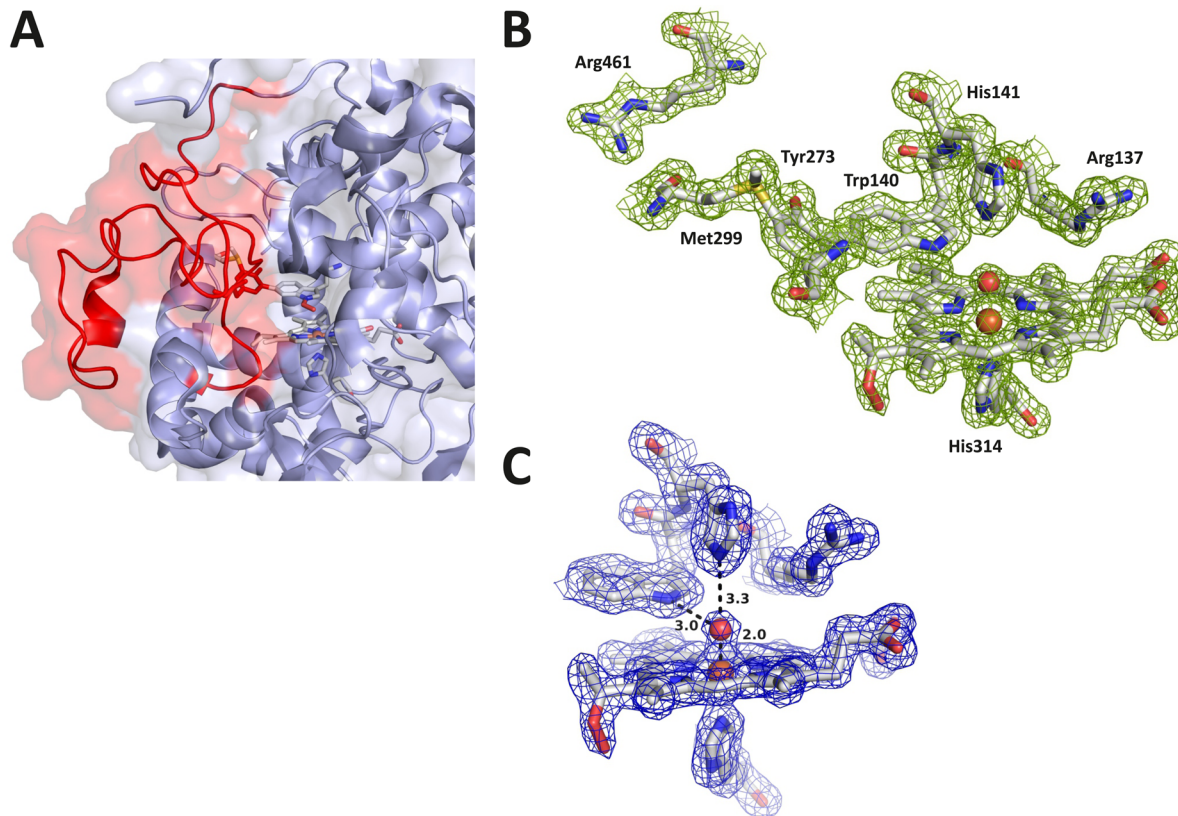


Figure 7. Crystal structure of an oxoiron state of *MagKatG2*. (A) Presentation of large loop 1 (LL1) (red) that includes Tyr273 of the Trp-Tyr-Met adduct. (B) View of the active site of wild-type *MagKatG2* soaked with peroxyacetic acid. The electron density map drawn at $\sigma = 1.0$ clearly shows the position of the catalytic residues, the adduct, and the mobile arginine (Arg461) being present exclusively in the “out” conformation away from the adduct. (C) Detailed view of the iron environment with distances between the oxoiron oxygen and heme iron, indole nitrogen of Trp140, and imidazole N ε 2 of His141. Figures were created with PyMOL (PyMOL Molecular Graphics System, version 1.3.0, Schrödinger, LLC).

MagKatG2-typical intersubunit disulfide bonds. As a consequence, the differences in rmsf and rsmd values (*Supplemental Figure 3*) are more pronounced in the N-terminal domain than in the C-terminal domain of both wild-type *MagKatG2* and Tyr273Phe. At first sight, this may seem to be contradictory to the unfolding experiments (see above). However, in the latter studies, the whole (disulfide-stabilized) dimeric protein was used.

Supplemental Figure 4 shows the first snapshot of MD simulations of the wild type or the Tyr273Phe mutant aligned with the most representative structure, which corresponds to the central member structure of the first conformational cluster (CMS1). The first and largest conformational clusters contained 54.9 and 22.5% of all occurring structures for the wild-type and the Tyr273Phe mutant, respectively, indicating the greater conformational flexibility of the mutant. The alignment clearly demonstrates conformational differences between wild-type *MagKatG2* (*Supplemental Figure 4A*) and the Tyr273Phe mutant (*Supplemental Figure 4B*). Among other differences, the secondary structure content of LL1 changed due to rearrangements in Tyr273Phe. Interestingly, the distance measurements at the constriction of the access channel to the heme cavity (i.e., fully conserved Asp and Ser) as well as at the outer part of the channel were only slightly increased.

■ DISCUSSION

MagKatG2 belongs to a novel group of eukaryotic catalase-peroxidases that contain signal sequences for secretion^{21,25} and are found almost exclusively in phytopathogenic fungi. The physiological role of the homologous protein from *Magnaporthe oryzae* has been analyzed and shown to be important in H₂O₂ detoxification for coping with the host oxidative burst.²⁸ It is reasonable to assume a similar role for KatG2 from the rice blast fungus *M. grisea*.

KatGs are unique because they are able to dismutate hydrogen peroxide like typical (monofunctional) catalases but appear in peroxidase clothing.⁴³ Because of an autocatalytically formed posttranslational modification, KatGs have two interdependently cooperating redox cofactors, namely, the prosthetic group heme b and in the proximity a peculiar adduct, formed by covalent bonds among fully conserved Trp140, Tyr273, and Met299. This unique structure could be verified by X-ray crystallography and mass spectrometry in prokaryotic KatGs^{5–7,10,11} as well as in recently found eukaryotic counterparts.^{8,27} Both spectral and structural studies suggest similar active site architecture in prokaryotic and eukaryotic KatGs,^{8,27,44} which is reflected by the determined standard reduction potential of the Fe(III)/Fe(II) couple of -210 mV for *MagKatG2*²⁷ that is in the range of those of its prokaryotic counterparts.^{45–47}

However, the extracellular eukaryotic enzyme also exhibits significant differences compared to bacterial or archaeal KatGs, including a more acidic optimum of the catalase activity (pH

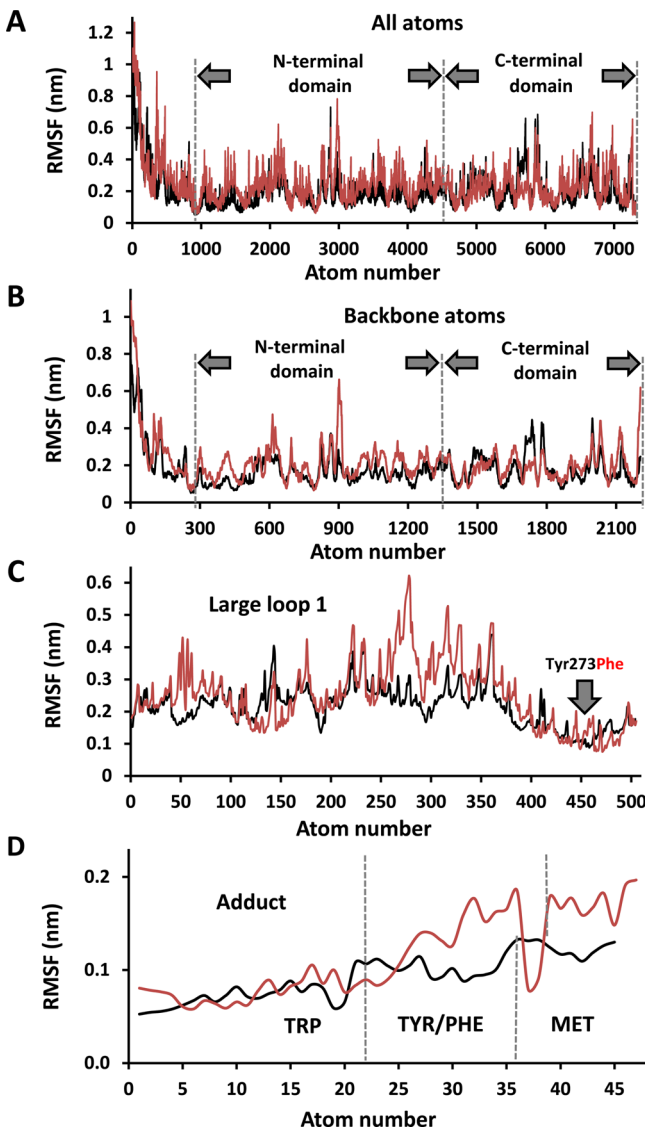


Figure 8. Comparison of molecular dynamics of wild-type *MagKatG2* and variant Tyr273Phe. Root-mean-square fluctuations (rmsfs) of all atoms (A), backbone atoms (B), large loop 1 (LL1) residues (C), and the three adduct residues (D). The rmsfs for wild-type *MagKatG2* and Tyr273Phe are drawn as black and red lines, respectively.

5.25) compared to that of the prokaryotic enzymes (around pH 6.0) as well as a significantly higher conformational and thermal stability due to wrapping at the dimer interface of the N-terminal elongations from the two subunits and cysteine residues that cross-link the two monomers.⁸ Elimination of this Cys55–Cys74 intersubunit disulfide bridge by alanine exchange decreases the thermal stability by more than 10 °C.⁸ It was interesting to see that disruption of the adduct leads to an even stronger destabilization of the protein. In both Trp140Phe and Tyr273Phe, the T_m values were decreased by more than 16 °C compared to that of wild-type *MagKatG2*. Because in all adduct variants the disulfide bridges were still established, this clearly underlines the importance of this posttranslational modification in the stability of KatG. The fact that the mutant protein Met299Ala is more stable than the other variants can easily be explained by the fact that this mutant still allows the autocatalytic production of a covalent bond between Trp140

and Tyr273 (and thus still anchors LL1) as demonstrated in prokaryotic KatGs.^{10,11}

The decrease in thermal stability that accompanies the loss of integrity of the adduct was nicely reflected by the increased flexibility of the Tyr273Phe variant compared to that of wild-type *MagKatG2* as shown by MD simulations. There was a clear increase in the rmsf of the overall mutant protein and especially at residues 228–279 (that constitute LL1) and Phe273 as well as Met299, but elimination of Tyr273 does not affect the conformation of Trp140, which due to π -stacking with the heme, keeps its wild-type position, which might explain the relatively small effect on the UV and EPR spectral properties of mutant proteins compared to those of wild-type *MagKatG2*.

Furthermore, disruption of the adduct and the resulting increased flexibility of LL1 enhance the accessibility of ligands and substrates to the active site. This effect is minor for small ligands but increases dramatically for larger molecules like peroxyacetic acid. The apparent rate of oxidation of the mutant Tyr273Phe by PAA was 230 times faster than that of the wild-type protein. Increased accessibility could also be responsible for the increase in peroxidase activity observed generally with adduct mutants in KatGs. It might also contribute to the decrease in *catalatic* activity, at least to some extent (although for the latter the role of the adduct as a second redox-active organic cofactor is more important as discussed below). For hydrogen peroxide-dismutating enzymes like KatGs and monofunctional catalases, a long and constricted main channel has been shown to be important. Hydrogen peroxide oxidation (but not H_2O_2 reduction) needs an ordered matrix of oriented water dipoles in the access channel. Its disruption results in modification of enthalpic and entropic contributions to the standard reduction potential of the Fe(III)/Fe(II) couple that clearly reflects reduction-induced changes in polarity, electrostatics, continuity, and accessibility of solvent to the metal center as well as alterations in solvent reorganization.⁴⁷ As a consequence, both KatGs and monofunctional catalases lose *catalatic* activity but gain *peroxidatic* activity upon disruption of the ordered matrix of water molecules.

Although the rate of oxidation of the ferric enzymes by PAA was different, the observed spectral transitions were similar in wild-type and mutant *MagKatG2*. Oxidation leads to rapid formation of Compound I [oxoiron(IV)porphyrin cation radical species] followed by slow one-electron reduction by the protein that becomes oxidatively modified.⁴⁰ As a consequence, Compound I*, an oxoiron compound with a remote protein radical site, is formed transiently. In this work, the presence of an oxoiron species of *MagKatG2* is strongly supported by the high-resolution X-ray structure with continuous electron density extending from the heme iron to a second atom, most probably oxygen, at distance of 2.0 Å. Structures of Compound I and Compound III-like species of monofunctional peroxidases⁴² show shorter oxo–iron distances (<1.73 Å). Therefore, the lengthened iron–oxo bond observed in this work most probably corresponds to a Compound I* state, formed by either migration of the porphyrin cation radical or photoreduction of Compound I, accompanied by protonation of the ferryl oxygen. Besides the oxygen modification of the heme iron, the vinyl group of pyrrole ring I shows a peculiar modification on the proximal side, which has never before been reported. A similar modification, though restricted to the distal heme side, was found in the first reported *BpKatG* structure.⁶ This points out the possibility for the heme group to react at

least transiently with reactive substrates or intermediates produced during catalytic turnover. Despite the differences in the vicinity of the heme, the overall appearance of the new *MagKatG2* structure, including important active site residues as well as the presence of water molecules in the tapered substrate channel, seems to be very similar to that of the reported wild-type structure.⁸

This first mechanistic study of a eukaryotic KatG clearly underlines the crucial role of the redox-active covalent adduct in the *pseudocatalytic* activity of catalase-peroxidases. As previously described for prokaryotic KatGs, disruption of the adduct leads to a dramatic decrease in the rate of hydrogen peroxide turnover. Although bifunctional catalase-peroxidases catalyze the same overall reaction as monofunctional catalases, they are structurally different and share their active site scaffold with monofunctional peroxidases. Thereby, efficient hydrogen peroxide oxidation by KatGs clearly follows a mechanism different from that in monofunctional catalases.

Initial hydrogen peroxide reduction with concomitant formation of an oxoiron(IV)porphyrin cation radical species $\{\text{Fe}(\text{IV})=\text{O} [\text{Por}]^{\bullet+}\}$, known as the Compound I state, renders the first step of both monofunctional catalases and peroxidases. Monofunctional catalases are able to catalyze the immediate reduction of this oxidation state by a second molecule of hydrogen peroxide, thereby re-establishing the ferric resting state and releasing molecular oxygen. In contrast to this efficient hydrogen peroxide dismutation, Compound I of monofunctional peroxidases cannot be reduced by hydrogen peroxide to the ferric state. Instead, they are known to get stuck in a Compound III state $\{\text{Fe}(\text{III})-\text{O}_2^{\bullet-}\} \leftrightarrow \{\text{Fe}(\text{II})-\text{O}_2\}$ upon being treated with an excess of hydrogen peroxide in the absence of appropriate electron donors, slowly releasing superoxide or negligible amounts of dioxygen.²²

For KatGs, it has been demonstrated that there is no direct reduction of Compound I with hydrogen peroxide.^{16,18,19} It has been shown that the first step after classical Compound I $\{\text{Fe}(\text{IV})=\text{O} [\text{Por}]^{\bullet+}\}$ formation is the conversion to a so-called Compound I* state.¹⁶ The entire covalent adduct (MYW) quenches the porphyrin radical forming this intermediate $\{\text{Fe}(\text{IV})=\text{O} [\text{MYW}]^{\bullet+}\}$ that is unique to catalase-peroxidases.^{18–20} Thereby, KatGs keep an oxidation equivalent in the adduct, very close to the heme iron, that might be important for the fast turnover of a second molecule of hydrogen peroxide. How exactly this adduct radical helps in the *pseudocatalytic* activity is still being discussed.

One possible route^{16,18–20} involves the formation of a Compound III-like state similar to monofunctional peroxidases. In an excess of hydrogen peroxide, monofunctional peroxidases get trapped in a Compound III state.²² KatGs are thought to keep their oxidation equivalent on the adduct and form a Compound III* $\{\text{Fe}(\text{II})-\text{O}_2 [\text{MYW}]^{\bullet+}\} \leftrightarrow \{\text{Fe}(\text{III})-\text{O}_2^{\bullet-} [\text{MYW}]^{\bullet+}\}$ intermediate. This Compound III* state finally decomposes very rapidly to release solely dioxygen and restore the ferric resting state as well as the closed shell covalent adduct.

A second described mechanism⁴⁸ is specified by two distinct proton/hydrogen transfers. The transfer of a hydrogen atom from the hydrogen peroxide to the oxoferryl is thought to restore the ferric nature [Fe(III)] of the heme iron. The second transfer of a proton from the adduct tryptophan to the [Fe(III)-OH] state allows release of a water molecule and formation of the hydroperoxide radical (-OOH) bound to the active site. Finally, release of dioxygen and protonation of the

adduct tryptophan restore both the ferric resting state and the adduct completely.⁴⁸

The important role of the adduct as a radical site can be modulated by a mobile arginine, found in the proximity of the covalent adduct, but more than 20 Å from the active site. Similar to the adduct residues, the exchange of this arginine resulted in a strongly decreased catalatic activity.^{15,20,41} It has been shown to adopt different conformations in a pH-dependent manner: an “in” conformation, pointing toward the hydroxyl group of the adduct tyrosine, or an “out” conformation, bending its side chain away from the adduct. This residue has a strong impact on the electronic properties of the adduct, thereby influencing its electron density and contributing to the reactivity of KatGs. Recent studies suggest the direct modulation of the adduct by the mobile arginine, thereby lowering the energy barrier for the radical transfer to the adduct.^{48,49}

In conclusion, this paper describes a detailed investigation of the role of the covalent adduct in a eukaryotic KatG (*MagKatG2*). As in prokaryotic KatGs, the intact adduct is a prerequisite for the *catalatic* activity of the enzyme. Spectral signatures during hydrogen peroxide turnover are consistent with the formation of a Compound III* species as previously observed in bacterial counterparts. Furthermore, we could show for the first time that the disruption of the adduct leads to a dramatic decrease in overall stability and an increase in flexibility, especially of large loop 1 involved in constriction of the tapered main access channel in KatGs.

■ ASSOCIATED CONTENT

S Supporting Information

The Supporting Information is available free of charge on the ACS Publications website at DOI: [10.1021/acs.biochem.5b00831](https://doi.org/10.1021/acs.biochem.5b00831).

Primers used for site-directed mutagenesis of *MagKatG2* (Supplemental Table 1), temperature-mediated unfolding monitored by circular dichroism spectroscopy (Supplemental Figure 1), reaction of wild-type and mutant proteins with cyanide (Supplemental Figure 2), rmsd with respect to the initial structure derived from 50 ns MD simulations (Supplemental Figure 3), and snapshots from MD simulations (Supplemental Figure 4) ([PDF](#))

Accession Codes

Atomic coordinates and structure factors have been deposited in the RCSB PDB as entry SCJH.

■ AUTHOR INFORMATION

Corresponding Author

*Phone: +43-1-47654-6073. Fax: +43-1-47654-6059. E-mail: christian.obinger@boku.ac.at.

Funding

This project was supported by the Austrian Science Foundation, FWF [Doctoral program BioToP-Biomolecular Technology of Proteins (W1224) and Projects P23855 and P25270].

Notes

The authors declare no competing financial interest.

ABBREVIATIONS

KatG, catalase-peroxidase; MagKatG2, secreted (extracellular) catalase-peroxidase from *M. grisea*; BpKatG, KatG from *B. pseudomallei*; MtKatG, KatG from *My. tuberculosis*; SynKatG, KatG from *Synechocystis* PCC6803; CD, circular dichroism; EPR, electron paramagnetic resonance; DSC, differential scanning calorimetry; MD, molecular dynamics; PAA, peroxyacetic acid.

REFERENCES

- (1) Zámocký, M., Gasselhuber, B., Furtmüller, P. G., and Obinger, C. (2012) Molecular evolution of hydrogen peroxide degrading enzymes. *Arch. Biochem. Biophys.* 525, 131–144.
- (2) Hillar, A., Peters, B., Pauls, R., Loboda, A., Zhang, H., Mauk, A. G., and Loewen, P. C. (2000) Modulation of the activities of catalase-peroxidase HPI of *Escherichia coli* by site-directed mutagenesis. *Biochemistry* 39, 5868–5875.
- (3) Regelsberger, G., Jakopitsch, C., Furtmüller, P. G., Rüker, F., Switala, J., Loewen, P., and Obinger, C. (2001) The role of distal tryptophan in the bifunctional activity of catalase-peroxidases. *Biochem. Soc. Trans.* 29, 99–105.
- (4) Jakopitsch, C., Auer, M., Ivancich, A., Rüker, F., Furtmüller, P. G., and Obinger, C. (2003) Total conversion of bifunctional catalase-peroxidase (KatG) to monofunctional peroxidase by exchange of a conserved distal side tyrosine. *J. Biol. Chem.* 278, 20185–20191.
- (5) Yamada, Y., Fujiwara, T., Sato, T., Igarashi, N., and Tanaka, N. (2002) The 2.0 Å crystal structure of catalase-peroxidase from *Haloarcula marismortui*. *Nat. Struct. Biol.* 9, 691–695.
- (6) Carpene, X., Loprasert, S., Mongkolsuk, S., Switala, J., Loewen, P. C., and Fita, I. (2003) Catalase-peroxidase KatG of *Burkholderia pseudomallei* at 1.7 Å resolution. *J. Mol. Biol.* 327, 475–489.
- (7) Bertrand, T., Eady, N. A., Jones, J. N., Jesmin, Nagy, J. M., Jamart-Grégoire, B., Raven, E. L., and Brown, K. A. (2004) Crystal structure of *Mycobacterium tuberculosis* catalase-peroxidase. *J. Biol. Chem.* 279, 38991–38999.
- (8) Zámocký, M., Garcia-Fernandez, M. Q., Gasselhuber, B., Jakopitsch, C., Furtmüller, P. G., Loewen, P. C., Fita, I., Obinger, C., and Carpene, X. (2012) High thermal and conformational stability of secretory eukaryotic catalase-peroxidases - Answers from first crystal structure and unfolding studies. *J. Biol. Chem.* 287, 32254–32262.
- (9) Kamachi, S., Wada, K., Tamoi, M., Shigeoka, S., and Tada, T. (2014) The 2.2 Å resolution structure of the catalase-peroxidase KatG from *Synechococcus elongatus* PCC7942. *Acta Crystallogr., Sect. F: Struct. Biol. Commun.* 70, 288–293.
- (10) Jakopitsch, C., Kolarich, D., Petutschnig, G., Furtmüller, P. G., and Obinger, C. (2003) Distal side tryptophan, tyrosine and methionine in catalase-peroxidases are covalently linked in solution. *FEBS Lett.* 552, 135–140.
- (11) Donald, L. J., Krokhin, O. V., Duckworth, H. W., Wiseman, B., Deemagarn, T., Singh, R., Switala, J., Carpene, X., Fita, I., and Loewen, P. C. (2003) Characterization of the catalase-peroxidase KatG from *Burkholderia pseudomallei* by mass spectrometry. *J. Biol. Chem.* 278, 35687–35692.
- (12) Regelsberger, G., Jakopitsch, C., Engleder, M., Rüker, F., Peschek, G. A., and Obinger, C. (1999) Spectral and kinetic studies of the oxidation of monosubstituted phenols and anilines by recombinant *Synechocystis* catalase - Peroxidase compound I. *Biochemistry* 38, 10480–10488.
- (13) Ghiladi, R. A., Medzihradzky, K. F., and Ortiz de Montellano, P. R. (2005) Role of the Met-Tyr-Trp cross-link in *Mycobacterium tuberculosis* catalase-peroxidase (KatG) as revealed by KatG (M25I). *Biochemistry* 44, 15093–15105.
- (14) Ghiladi, R. A., Knudsen, G. M., Medzihradzky, K. F., and Ortiz de Montellano, P. R. (2005) The Met-Tyr-Trp cross-link in *Mycobacterium tuberculosis* catalase-peroxidase (KatG): autocatalytic formation and effect on enzyme catalysis and spectroscopic properties. *J. Biol. Chem.* 280, 22651–22663.
- (15) Jakopitsch, C., Ivancich, A., Schmuckenschlager, F., Wanasinghe, A., Pöltl, G., Furtmüller, P. G., Rüker, F., and Obinger, C. (2004) Influence of the unusual covalent adduct on the kinetics and formation of radical intermediates in *Synechocystis* catalase peroxidase: a stopped-flow and EPR characterization of the MET275, TYR249, and ARG439 variants. *J. Biol. Chem.* 279, 46082–46095.
- (16) Jakopitsch, C., Vlasits, J., Wiseman, B., Loewen, P. C., and Obinger, C. (2007) Redox intermediates in the catalase cycle of catalase-peroxidases from *Synechocystis* PCC 6803, *Burkholderia pseudomallei*, and *Mycobacterium tuberculosis*. *Biochemistry* 46, 1183–1193.
- (17) Yu, S., Girotto, S., Zhao, X., and Magliozzo, R. S. (2003) Rapid formation of compound II and a tyrosyl radical in the Y229F mutant of *Mycobacterium tuberculosis* catalase-peroxidase disrupts catalase but not peroxidase function. *J. Biol. Chem.* 278, 44121–44127.
- (18) Suarez, J., Rangue洛va, K., Jarzecki, A. A., Manzerova, J., Krymov, V., Zhao, X., Yu, S., Metlitsky, L., Gerfen, G. J., and Magliozzo, R. S. (2009) An oxyferrous heme/protein-based radical intermediate is catalytically competent in the catalase reaction of *Mycobacterium tuberculosis* catalase-peroxidase (KatG). *J. Biol. Chem.* 284, 7017–7029.
- (19) Zhao, X., Suarez, J., Khajo, A., Yu, S., Metlitsky, L., and Magliozzo, R. S. (2010) A radical on the Met-Tyr-Trp modification required for catalase activity in catalase-peroxidase is established by isotopic labelling and site-directed mutagenesis. *J. Am. Chem. Soc.* 132, 8268–8269.
- (20) Zhao, X., Khajo, A., Jarrett, S., Suarez, J., Levitsky, Y., Burger, R. M., Jarzecki, A. A., and Magliozzo, R. S. (2012) Specific function of the Met-Tyr-Trp adduct radical and residues Arg-418 and Asp-137 in the atypical catalase reaction of catalase-peroxidase KatG. *J. J. Biol. Chem.* 287, 37057–37065.
- (21) Zámocký, M., Furtmüller, P. G., and Obinger, C. (2010) Evolution of structure and function of Class I peroxidases. *Arch. Biochem. Biophys.* 500, 45–57.
- (22) Vlasits, J., Jakopitsch, C., Bernroitner, M., Zámocký, M., Furtmüller, P. G., and Obinger, C. (2010) Mechanisms of catalase activity of heme peroxidases. *Arch. Biochem. Biophys.* 500, 74–81.
- (23) Passardi, F., Zámocký, M., Favet, J., Jakopitsch, C., Penel, C., Obinger, C., and Dunand, C. (2007) Phylogenetic distribution of catalase-peroxidases: are there patches of order in chaos? *Gene* 397, 101–113.
- (24) Zámocký, M., Furtmüller, P. G., and Obinger, C. (2008) Evolution of catalases from bacteria to humans. *Antioxid. Redox Signaling* 10, 1527–1548.
- (25) Zámocký, M., Furtmüller, P. G., and Obinger, C. (2009) Two distinct groups of fungal catalase/peroxidases. *Biochem. Soc. Trans.* 37, 772–777.
- (26) Zámocký, M., Furtmüller, P. G., Bellei, M., Battistuzzi, G., Stadlmann, J., Vlasits, J., and Obinger, C. (2009) Intracellular catalase/peroxidase from the phytopathogenic rice blast fungus *Magnaporthe grisea*: expression analysis and biochemical characterization of the recombinant protein. *Biochem. J.* 418, 443–451.
- (27) Zámocký, M., Droghetti, E., Bellei, M., Gasselhuber, B., Pabst, M., Furtmüller, P. G., Battistuzzi, G., Smulevich, G., and Obinger, C. (2012) Eukaryotic extracellular catalase-peroxidase from *Magnaporthe grisea*: biophysical/chemical characterization of the first representative from a novel phytopathogenic KatG group. *Biochimie* 94, 673–683.
- (28) Tanabe, S., Ishii-Minami, N., Saitoh, K., Otake, Y., Kaku, H., Shibuya, N., Nishizawa, Y., and Minami, E. (2011) The role of catalase-peroxidase secreted by *Magnaporthe oryzae* during early infection of rice cells. *Mol. Plant-Microbe Interact.* 24, 163–171.
- (29) Schmid, N., Christ, C. D., Christen, M., Eichenberger, A. P., and van Gunsteren, W. F. (2012) Architecture, implementation and parallelisation of the GROMOS software for biomolecular simulation. *Comput. Phys. Commun.* 183, 890–903.
- (30) Schmid, N., Eichenberger, A. P., Choutko, A., Riniker, S., Winger, M., Mark, A. E., and van Gunsteren, W. F. (2011) Definition and testing of the GROMOS force-field versions: 54A7 and 54B7. *Eur. Biophys. J.* 40, 843–856.

- (31) Berendsen, H. J. C., Postma, J. P. M., Van Gunsteren, W. F., and Hermans, J. (1981) Interaction models for water in relation to protein hydration. *Intermolecular Forces*, 331–342.
- (32) Amadei, A., Chillemi, G., Ceruso, M. A., Grottesi, A., and Di Nola, A. (2000) Molecular dynamics simulations with constrained roto-translational motions: Theoretical basis and statistical mechanical consistency. *J. Chem. Phys.* 112, 9–23.
- (33) Berendsen, H. J. C., Postma, J. P. M., van Gunsteren, W. F., Di Nola, A., and Haak, J. R. (1984) Molecular dynamics with coupling to an external bath. *J. Chem. Phys.* 81, 3684–3690.
- (34) Ryckaert, J.-P., Ciccotti, G., and Berendsen, H. J. (1977) Numerical integration of the cartesian equations of motion of a system with constraints: molecular dynamics of n-alkanes. *J. Comput. Phys.* 23, 327–341.
- (35) Tironi, I. G., Sperb, R., Smith, P. E., and van Gunsteren, W. F. (1995) A generalized reaction field method for molecular dynamics simulations. *J. Chem. Phys.* 102, 5451–5459.
- (36) Heinz, T. N., van Gunsteren, W. F., and Hünenberger, P. H. (2001) Comparison of four methods to compute the dielectric permittivity of liquids from molecular dynamics simulations. *J. Chem. Phys.* 115, 1125–1136.
- (37) Daura, X., van Gunsteren, W. F., and Mark, A. E. (1999) Folding-unfolding thermodynamics of a beta-heptapeptide from equilibrium simulations. *Proteins: Struct., Funct., Genet.* 34, 269–280.
- (38) Zámocký, M., Hofbauer, S., Schaffner, I., Gasselhuber, B., Nicolussi, A., Soudi, M., Pirker, K. F., Furtmüller, P. G., and Obinger, C. (2015) Independent evolution of four heme peroxidase superfamilies. *Arch. Biochem. Biophys.* 574, 108–119.
- (39) Zamocký, M., Regelsberger, G., Jakopitsch, C., and Obinger, C. (2001) The molecular peculiarities of catalase-peroxidases. *FEBS Lett.* 492, 177–182.
- (40) Ivancich, A., Donald, L. J., Villanueva, J., Wiseman, B., Fita, I., and Loewen, P. C. (2013) Spectroscopic and kinetic investigations of the reactions of peroxyacetic acid *Burkholderia pseudomallei* catalase-peroxidase, KatG. *Biochemistry* 52, 7271–7282.
- (41) Carpena, X., Wiseman, B., Deemagarn, T., Singh, R., Switala, J., Ivancich, A., Fita, I., and Loewen, P. C. (2005) A molecular switch and electronic circuit modulate catalase activity in catalase-peroxidases. *EMBO Rep.* 6, 1156–1162.
- (42) Gumiero, A., Metcalfe, C. L., Pearson, A. R., Raven, E. L., and Moody, P. C. E. (2011) Nature of the ferryl heme in compounds I and II. *J. Biol. Chem.* 286, 1260–1268.
- (43) Njuma, O. J., Ndontsa, E. N., and Goodwin, D. C. (2014) Catalase in peroxidase clothing: Interdependent cooperation of two cofactors in the catalytic versatility of KatG. *Arch. Biochem. Biophys.* 544, 27–39.
- (44) Smulevich, G., Jakopitsch, C., Droghetti, E., and Obinger, C. (2006) Probing the structure and bifunctionality of catalase-peroxidase (KatG). *J. Inorg. Biochem.* 100, 568–585.
- (45) Bellei, M., Jakopitsch, C., Battistuzzi, G., Sola, M., and Obinger, C. (2006) Redox thermodynamics of the ferric-ferrous couple of wild-type *Synechocystis* KatG and KatG (Y249F). *Biochemistry* 45, 4768–4774.
- (46) Battistuzzi, G., Bellei, M., Bortolotti, C. A., and Sola, M. (2010) redox properties of heme peroxidases. *Arch. Biochem. Biophys.* 500, 21–36.
- (47) Vlasits, J., Bellei, M., Jakopitsch, C., De Rienzo, F., Furtmüller, P. G., Zamocký, M., Sola, M., Battistuzzi, G., and Obinger, C. (2010) Disruption of the H-bond network in the main access channel of catalase-peroxidase modulates enthalpy and entropy of Fe(III) reduction. *J. Inorg. Biochem.* 104, 648–656.
- (48) Loewen, P. C., Carpena, X., Vidossich, P., Fita, I., and Rovira, C. (2014) An ionizable active-site tryptophan imparts catalase activity to a peroxidase core. *J. Am. Chem. Soc.* 136, 7249–7252.
- (49) Kruft, B. I., Magliozzo, R. S., and Jarzecki, A. A. (2015) Density Functional Theory Insights into the role of the methionine-tyrosine-tryptophan adduct radical in the KatG catalase reaction: O₂ release from the oxyheme intermediate. *J. Phys. Chem. A* 119, 6850–6866.
- (50) Singh, R., Wiseman, B., DeeMagarn, T., Jha, V., Switala, J., and Loewen, P. C. (2008) Comparative study of catalase-peroxidases (KatGs). *Arch. Biochem. Biophys.* 471, 207–214.
- (51) Singh, R., Wiseman, B., DeeMagarn, T., Donald, L. J., Duckworth, H. W., Carpena, X., Fita, I., and Loewen, P. C. (2004) Catalase-peroxidases (KatG) exhibit NADH oxidase activity. *J. Biol. Chem.* 279, 43098–43106.